

## Article

# Flow Field around a Vertical Cylinder in Presence of Long Waves: An Experimental Study

Rosangela Basile <sup>1</sup> and Francesca De Serio <sup>1,2,\*</sup> 

<sup>1</sup> DICATECH, Department of Civil, Environmental, Land, Building Engineering and Chemistry, Polytechnic University of Bari, 70125 Bari, Italy; rosangela.basile@poliba.it

<sup>2</sup> CoNISMa-Interuniversity Consortium for Marine Sciences, 00196 Rome, Italy

\* Correspondence: francesca.deserio@poliba.it; Tel.: +39-080-5963557

**Abstract:** Long waves caused by storm surges or river floods can significantly impact marine and fluvial structures such as bridge piers. Apart from the forces that they generate on the structure, they also contribute to the formation of turbulent eddies downstream of the obstacle. This is relevant, as in this way they can affect both an erodible bottom and the ecosystem. The present study describes a medium-scale experiment, in which the propagation of two different long waves released on a steady current is investigated in the presence of a bottom-mounted rigid emergent cylinder. Velocity measurements were acquired by a Particle Image Velocimetry (PIV) system, providing instantaneous flow velocity vectors on selected 2D planes. For each experimental condition, the time-varying velocity field near the cylinder was examined in selected vertical and horizontal planes. First, we tested which analytical theory or approximated method can best represent the experimental waves. After this, we estimated the horizontal maps of velocity and vorticity downstream of the obstacle and finally processed the velocity signals by means of a wavelet-based technique, to derive the length scales of turbulent eddies. In such a way, we specifically derived how the spreading of coherent turbulent structures downstream of the cylinder depends on the features of the flume, cylinder, and wave.



**Citation:** Basile, R.; De Serio, F. Flow Field around a Vertical Cylinder in Presence of Long Waves: An Experimental Study. *Water* **2022**, *14*, 1945. <https://doi.org/10.3390/w14121945>

Academic Editor: Giuseppe Pezzinga

Received: 27 May 2022

Accepted: 15 June 2022

Published: 17 June 2022

**Publisher's Note:** MDPI stays neutral with regard to jurisdictional claims in published maps and institutional affiliations.



**Copyright:** © 2022 by the authors. Licensee MDPI, Basel, Switzerland. This article is an open access article distributed under the terms and conditions of the Creative Commons Attribution (CC BY) license (<https://creativecommons.org/licenses/by/4.0/>).

**Keywords:** solitary wave; turbulent coherent structures; length scales; wavelet transform

## 1. Introduction

In a marine and fluvial environment, civil infrastructures are often exposed to extreme wave actions. This is certainly the case of coastal and offshore facilities during storm surges, as well as of riverine bridge piers when a flood occurs. These events, typical of extreme conditions, are becoming more and more frequent and dangerous with climate change. Therefore, to provide proper structural designs and safety assessments, we must evaluate the impact of such extreme waves on these structures [1]. Generally, many experimental and numerical investigations have focused on the detection of both drag and inertia forces exerted by a flow on a vertical cylinder using the well-known Morison equation [2], requiring the detailed knowledge of the velocity field in which the cylinder is immersed.

Specifically, current–structure interaction and wave–structure interaction have been extensively examined, but separately. Among the many, Zdravkovich [3] defined the regions of disturbed flow field around a circular cylinder; Rockwell [4] characterized the spanwise flow structure around the cylinder in terms of instantaneous velocity and vorticity; Vested et al. [5] analyzed the force distribution on a vertical, circular cylinder exposed to shoaling regular waves; Antolloni et al. [6] investigated the wave-induced vortex generation around a slender, vertical cylinder; Duan et al. [7] described the shedding of vortices and the hydrodynamic forces resulting from a wave passing over a submerged circular cylinder; Chen and Wang [8] investigated with experiments and computations the wave interaction with fixed, partially submerged, vertical cylinders; Mo and Jensen [9] performed laboratory

experiments and numerical tests for solitary waves breaking on a constant slope, where a vertical cylinder was installed to detect the horizontal velocity profiles. More complex structures have also been examined in presence of waves, especially to evaluate their effect in reducing the transmitted energy [10,11]. Nevertheless, limited studies have investigated the joint wave–current–structure interaction. Further, when the mutual effects of all these three components have been considered, the waves analyzed were mainly regular ones. On the contrary, based on their great lengths and periods, extreme waves are often assumed as solitary waves. Only more recent research has addressed the interaction of the solitary wave with pile structures in experimental terms and in numerical terms. As an example, Yang et al. [12] carried out a series of experiments on a solitary wave–current interaction in the presence of a vertical obstacle, focusing on the changes in wave height and water velocity. Kim et al. [13] conducted numerical simulations of a wave and current interacting with fixed offshore substructures.

It is thus clear that more investigations are needed to better understand the mechanism of the interaction between wave, current, and structure. For this reason, the present study has a twofold purpose. Firstly, we aim at contributing to this deepening of knowledge by providing a set of high-quality experimental data for solitary waves travelling on a shallow current and interfering with vertical, bottom-mounted, rigid cylindrical structures. Secondly, we aim at analyzing in detail how the flow field downstream of the obstacle is affected by the transit of the wave in terms of vorticity and turbulence. In particular, we used medium-scale laboratory models and focused on the time-varying velocity field (i) upstream of the cylinder due to the wave transit, and (ii) downstream of the cylinder due to both the wave transit and the presence of the obstruction. Specifically, the first analysis is needed to detect how the velocity distribution changes due to the contemporary presence of waves and currents, while the second is dedicated to the observation of vorticity and coherent turbulent eddies that detach and spread from the cylinder. The underlying motivation is to contribute to a thorough knowledge of the distribution of eddies downstream, characterized by different length scales. In fact, it is well-known that the condition of incipient movement of sediment particles is significantly influenced by turbulent eddies given that they can penetrate up to the channel bed [14,15]. Moreover, resembling the transport of turbulent kinetic energy, eddies can contribute to the entrainment and transport of sediments or eventually tracers, thus they can affect a mobile bottom or even the biota and the local ecosystem [16,17].

This study is arranged as follows: in the next section we introduce the experimental setup used for the investigation and the theoretical frame for the wave's description. In Section 3, first the main features of the streamwise velocities are depicted and compared with the available theories to define the best matching one based on a proper index. After this, the vertical profiles of the flow velocity are examined during the wave transit. Further, vorticity and coherent turbulent structures in the horizontal plane around the cylinder are examined. Finally in Section 4 the main conclusions are summarized.

## 2. Materials and Methods

### 2.1. Experimental Equipment and Procedure

We performed the experiments at the Hydraulic Laboratory of the DICATECH of the Polytechnic University of Bari (Italy). The used rectangular flume, 25 m long and 0.4 m wide, has sidewalls and bottom fabricated of Plexiglass and is well-suited for optical measurements (Figure 1). The head tank feeding the flume can be served independently by both a low-pressure and a high-pressure water circuit. The low-pressure main circuit provided a stationary flow condition in the flume during the test (base flow). The high-pressure adduction pipe released an additional water discharge in the head tank by means of an electro valve (Figure 1) managed by a process PC, equipped with a LabVIEW software. In this way, by conveniently tuning the added water release, the desired long wave was generated in the channel, superimposed to the uniform base flow. At the downstream end of the channel, a second tank is located, receiving the discharged flow. It is provided with a

triangular sharp-crested weir used to estimate the flow rate. The water level is controlled by a sloping gate at the end of the flume. In order to reduce the reflection of the generated waves, a structure with a high degree of porosity, consisting of a 2 m in length metal cage with a 0.01 m mesh filled with  $d_{50} = 0.015$  m gravel, is located in the final part of the flume on the bottom. However, the measurements of the tested waves were acquired in a time period specifically chosen to avoid any reflection.

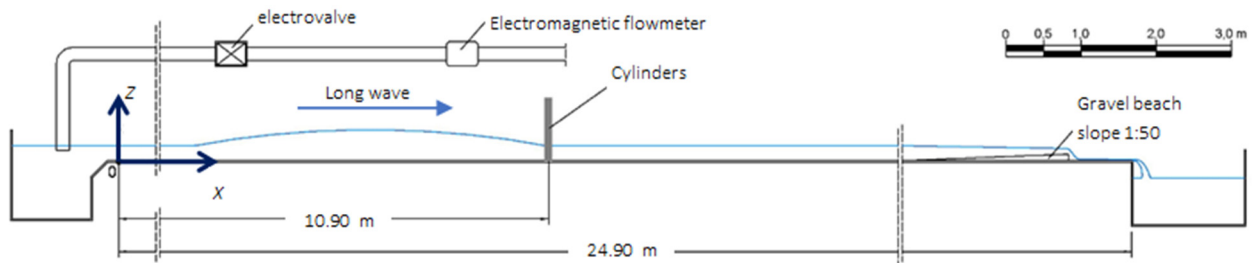


**Figure 1.** Sketch of the channel with location of the cylinders and (X,Z) axes. Side view.

The physical model was designed to reproduce a possible bridge pile affected by a river flood, in Froude analogy, thus using a length scale factor equal to 1/10 (model/prototype). Therefore, two rigid cylinders having a diameter  $d = 0.02$  m were located along the Y axis in the same transversal section, at a distance of  $X = 10.9$  m from the head tank O (X being the longitudinal axis of symmetry of the channel as in Figure 1). They were equidistant from the X axis, with  $Y = 0.10$  m and  $Y = -0.10$  m, respectively (Figure 2).

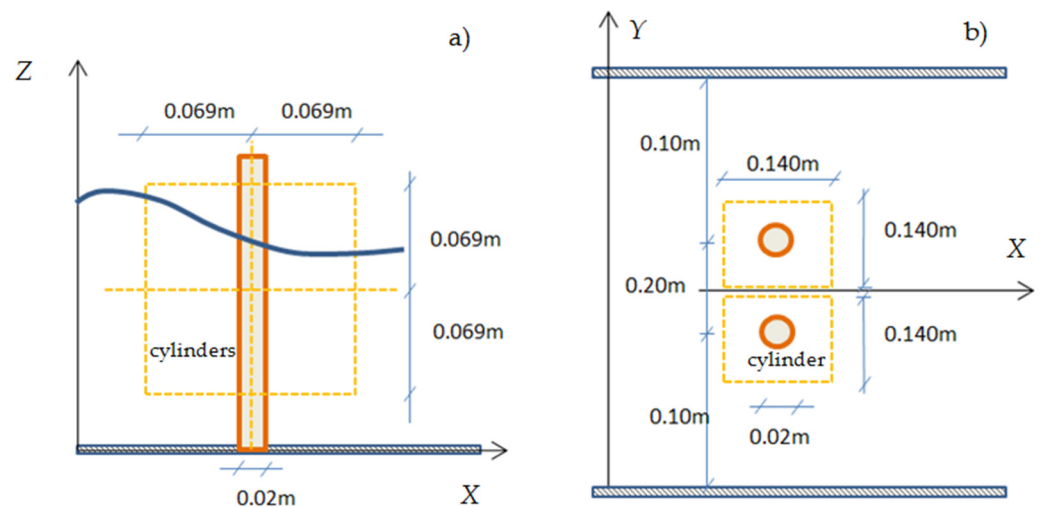


**Figure 2.** Sketch of the longitudinal (a) and plan view (b) of the cylinders in the flume with the fixed coordinate system (X,Y,Z). Dashed lines define the field of views (FoV) of the PIV. Measurements not to scale.

In order to obtain the flow velocity vectors on selected 2D planes, the velocity measurements were acquired by a Particle Image Velocimetry (PIV) technique. The 2D PIV system was equipped with a FlowSense EO 4M-32 camera, a laser with pulse energy of 200 mJ at 15 Hz and a synchronizer, controlled and monitored by a PC. The system was handled in double-frame mode; the sampling frequency was settled to 8.13 Hz and the time interval between two frames of the same pair was 150  $\mu$ s. Considering the importance of seeding particles to obtain good quality measurements [18], we used a neutrally buoyant silver powder as seeding tracer with a mean diameter of  $O(10 \mu$ m).

The data examined in the present work refer to the flow velocity (i) measured in the vertical plane (X,Z) at  $Y = 0.10$  m (Figure 2a), (ii) and measured in the horizontal plane (X,Y) located at  $Z = 0.03$  m from the bottom. The velocity components are:  $u$  along X, positive towards the gravel beach;  $v$  along Y, positive following Y;  $w$  along Z, positive upwards,

being  $Z = 0$  m at the channel bottom. The field of views (FoVs) were properly selected (see dashed squares in Figure 2). The interrogation area of the images in the adaptive correlation processing was  $32 \times 32$  pixels, thus the velocity vectors were assessed in points regularly spaced at 0.4 mm in the vertical plane and 0.8 mm in the horizontal one, resulting in a high spatial resolution. The number of such grid points for each FoV was  $172 \times 172$ , so the calibrated PIV images had the dimensions 69 mm  $\times$  69 mm and 138 mm  $\times$  138 mm, respectively, in the vertical and horizontal plane. Considering a precision in estimating the displacement within an interrogation window of 0.1 pixel, the accuracy for the detected PIV velocity was close to 1%.

The water depth in the flume was always set to be  $h = 0.1$  m. The base flow rate calculated with the Thomson-type triangular weir provided a reference base flow velocity  $u_0$  equal to 0.16 m/s for all the tests. The base flow Froude number and Reynolds number were  $Fr_0 = u_0/\sqrt{gh} = 0.162$  and  $Re_0 = u_0B/\nu = 64,000$ , respectively, thus representing a turbulent subcritical condition. The water kinematic viscosity  $\nu$  was set  $10^{-6}$  m<sup>2</sup>/s, while  $B$  was the channel width.

In order to replicate a flooding wave impacting a bridge pile two different long waves were examined in the experiments named W1 and W2, respectively. Each one was generated by linearly opening and successively closing the electro-valve of the high-pressure circuit (Figure 1) for a specific temporal interval. They were characterized by a wave height  $H$ , wave period  $T$ , wavelength  $L$ , and an Ursell number (index of non-linearity)  $Ur = HL/h^2$ , as shown in Table 1. The number of images acquired by the PIV was limited by technical reasons related to the storage size of the dedicated PC, thus it was set to 150 for each measurement. Consequently, the total acquisition time for each measurement was close to 18 s, which is lower than the entire wave periods. Nevertheless, it was sufficient to capture most of the ascending and descending part of each examined wave.

**Table 1.** Characteristics of the two tests.

Test	$H$ [m]	$T$ [s]	$L$ [m]	$Ur$ [-]
W1	0.025	20	32	80
W2	0.05	19	25	125

For both W1 and W2 tests, eight identical waves were generated and successively released in the flume, each of them separated from the previous one by the time-interval necessary to reconfigure the undisturbed condition in the channel. In this way, we could operate a phase averaging technique on the measured velocity signals [17] and obtain the turbulent fluctuations, as written in the following.

Finally, it is worth noting that in our physical model the spacing between the cylinders was 10 times their diameter, and thus each cylinder behaved as isolated, not affecting the flow field around the other one. Rather, a symmetry with respect to the longitudinal  $X$  axis in the flow was detected. This motivated our choice to focus our current analysis only on one cylinder, specifically on cylinder 2 (Figure 2).

## 2.2. Theoretical Background for Waves Description

To describe analytically the generated waves, based on their shape and featuring parameters, we referred to shallow waters following the classical definition [19]. In fact, in our case, the ratio between the water depth and the wavelength is  $h/L = 0.0008$  for W1 and  $h/L = 0.002$  for W2, i.e., less than  $1/25 = 0.04$ .

For this scope, we used the Korteweg–de Vries equation [20] originally derived to describe shallow water waves of great wavelength and small amplitude, thus having  $h \ll L$ , and  $H/h \ll 1$ . Its solution provides the time-varying orbital velocity component  $u$  along the wave propagation direction  $x$ :

$$u(x_i, t) = \frac{\omega - 4k^3(2m - 1)}{\alpha k} + \frac{12k^2 m}{\alpha} cn^2(kx_i - \omega t + \delta; m) \quad (1)$$

where  $k = 2\pi/L$  is the wave number,  $\omega = 2\pi/T$  is the angular frequency,  $\delta$  is the phase and  $\alpha$  is a parameter that can be scaled to any real number (but generally posed  $\pm 1$  and  $\pm 6$ ) [20]. It is called the cnoidal wave solution for it involves the Jacobi elliptic cosine function,  $cn$  with modulus  $m$  (where  $m = 0 \div 1$ ). Specifically, when  $m$  tends to zero, Equation (1) describes the Airy linear (LIN) wave [19]. On the contrary, when  $m = 1$ , Equation (1) describes a solitary wave with a finite amplitude and propagating entirely above the mean water level with constant speed and without change in shape over a fairly long distance.

As an alternative solitary wave solution, we considered the regularized long-wave equation proposed by Peregrine (PER) to describe the behavior of an undular bore with a smooth wavefront and having the following expression [20]:

$$u(x_i, t) = \frac{\omega - k - 4k^2\omega}{\alpha k} + \frac{12k\omega}{\alpha} \text{sech}^2(kx_i - \omega t + \delta) \quad (2)$$

Moreover, the classical solitary solution of the Boussinesq equation (BOU) was applied in our study [21]:

$$u(x_i, t) = \frac{\omega^2 - c^2k^2 - 4\beta k^2}{\alpha k^2} + \frac{12\beta k^2}{\alpha} \text{sech}^2(kx_i - \omega t + \delta) \quad (3)$$

where typically one sets  $\alpha = 3$  and  $\beta = 1$ , while  $c$  is the wave celerity.

Finally, we proposed to test an engineering method not tailored on shallow waters, but widely used in practice due to its simplicity, that is the so-called linear Wheeler stretching (WH) method [22]. It attempts to correct the linear Airy theory, whose straight application is valid from sea bottom to mean water level, by stretching the vertical coordinate  $Z$  up to the instantaneous free surface. Thus, a transfer function between wave elevation  $\eta$  and velocity components in the time domain is provided. As for the  $u$  component, we have:

$$u(x_i, Z, t) = \frac{\pi H}{T} \frac{\cosh k[Z/(1 + \eta(x, t)/h)]}{\sinh(kh)} \cos(kx_i - \omega t) \quad (4)$$

In the present study, due to some technical limitation during the experiments, wave elevations were not assessed; therefore, we substituted in Equation (4) the exact solitary wave elevation expression computed as [21]:

$$\eta(x_i, t) = H \text{sech}^2 \left[ \frac{1}{h} \sqrt{\frac{3H}{4h}} (x_i - ct) \right] \quad (5)$$

### 3. Results and Discussion

The results displayed in the following are based on the vector field maps assessed from pairs of PIV particle images by means of the adaptive correlation method, as implemented in data processing.

#### 3.1. Analytical Characterization of the Experimental Waves

The models described in Section 2.2 were taken into account and their reliability in reproducing the experimental waves generated was tested. To allow a consistent comparison between theoretical and experimental waves, we specifically referred to the streamwise velocity component  $u$ , suitably treated. Considering a fixed position (in our case  $x_i = X$ ), we computed  $u(t)$  through all the aforementioned analytical models. We used the following procedure for both cases W1 and W2 to extract the velocity measurements for the wave cycle from the experimental time series. We examined the streamwise velocity measured in a large number of points distant and undisturbed by the cylinders, both in the vertical plane upstream (Figure 2a) and in the horizontal plane (Figure 2b). For each measure-

ment, the phase averaging technique was used to process the  $u(t)$  signal, so that it was decomposed in a time-averaged value  $U$ , a phase-averaged value  $u_p(t)$  and a turbulent fluctuation  $u'(t)$  [17]. The ensemble-averaged value  $\langle u(t) \rangle$  was also taken into account with the sum  $\langle u(t) \rangle = U + u_p(t)$ . This phase averaging operation was applied to the eight waves measured, even if the assumption made of a solitary wave actually implies a non-periodical wave. We decided to follow this procedure because in this way (i) we could account for more robust and consistent measurements, not referring to a single episodic wave event, (ii) and we could operate statistics and extract turbulent components from the signal. Consequently, we were able to compare the trends of the theoretical  $u$  varying in the wave cycle with the corresponding phase-averaged experimental values  $u_p$ . As an example, for a selected point representative of the undisturbed hydrodynamic condition (far from the cylinder C2 and having coordinates  $X = 10.95$  m,  $Y = 0.07$  m and  $Z = 0.035$  m), Figure 3 shows the comparison among the computed values of  $u$  and the measured  $u_p$  (normalized by the time-averaged velocity  $U$ ). The time-averaged velocity in the two experiments is  $U = 0.28$  m/s for W1 and  $U = 0.40$  m/s for W2, respectively.

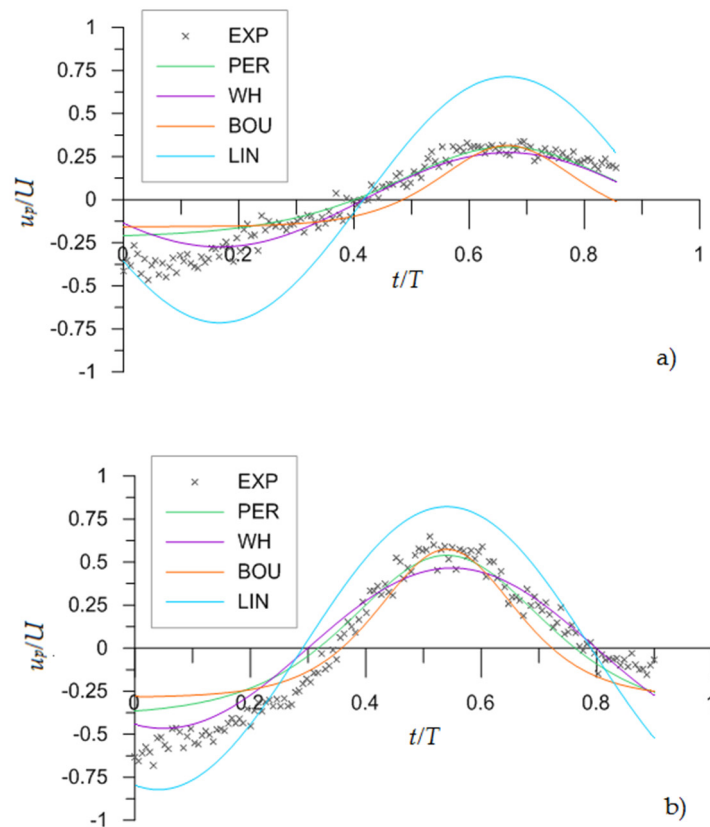


**Figure 3.** Comparison of computed  $u$  and experimental phase-averaged streamwise velocity  $u_p$  at point  $X = 10.95$  m,  $Y = 0.07$  m, and  $Z = 0.035$  m for W1 (a) and W2 (b).

In qualitative terms, for both waves W1 and W2, the WH method seems to show the best matching with the experimental data, while the linear model provides the largest overestimations in absolute terms. To evaluate the agreement also in quantitative terms, the Wilmott index  $Iw$  was considered [23]:

$$Iw = 1 - \frac{\sum_{i=1}^N (\chi_{ci} - \chi_i)^2}{\sum_{i=1}^N (|\chi_{ci} - \bar{\chi}| + |\chi_i - \bar{\chi}|)^2} \tag{6}$$

where  $\chi_c$  and  $\chi$  are, respectively, the computed and the experimental values; the overbar stands for the corresponding average value; and  $N$  is the total number of data in a wave cycle. The  $Iw$  index takes a value of 1 when a perfect agreement is obtained. If calculated for the whole wave cycle, it provides the highest values for the WH method for both W1 and W2 waves, resulting  $Iw = 0.99$  and  $Iw = 0.97$ , respectively.

In any case, at a closer inspection, a worse agreement can be observed between the measured data and the WH data during the wave crest transit. Thus, we also computed  $Iw$  for partial data intervals, namely for the positive velocity values (typical of the wave crest transit) and for the negative velocity values (typical of the wave trough transit). The resulting indexes are shown in Table 2.

**Table 2.** Wilmott index for comparisons of the streamwise velocity trends shown in Figure 3.

$Iw$	PER	WH	BOU	LIN
W1 trough	0.95	0.97	0.90	0.86
W1 crest	0.94	0.95	0.86	0.70
W2 trough	0.87	0.91	0.80	0.80
W2 crest	0.99	0.98	0.98	0.92

It is evident that for wave W1, the WH method is the best suited one along the whole wave cycle. For wave W2, it remains the best referring to the wave trough; while for the wave crest case, the PER model better reproduces the velocities  $u_p$ . It is worth noting that we obtain analogous results (within  $\pm 2\%$ , i.e., comparable to PIV accuracy) even when experimental velocities are examined at other undisturbed points. Finally, these results are also consistent with Iwagaki's abacus [15].

### 3.2. Upstream Vertical Profiles of the Streamwise Velocity

For both W1 and W2 waves, we analyzed the FoVs in the vertical plane, upstream the cylinder (Figure 2a). The flow field was observed both in stationary condition (i.e., base flow) and in wave condition, during the transit of the long wave. The vertical profiles of the ensemble-averaged velocity display a quite flat and uniform trend along most  $Z$ , during each phase of the wave. Apart from the typical values of the ratio  $h/L$  and the indications of Iwagaki's abacus already written in Section 2.2, it was this observation that led us to address theoretically shallow water waves characterized by a condition of homogeneous flow along  $Z$ . The rapid release of the added mass into the laboratory flume head tank produced a long flooding wave that promptly affected the entire water depth from the most superficial layer towards the channel bottom. The effect of the bottom on the flow is most visible during the descending wave phase when a reduction in velocity is generally assessed over the entire depth, but is even faster in the range  $Z/h < 0.4$ . In this range, for both waves, the logarithmic trend typical of uniform flow in open channels is identifiable.

Figure 4 displays, as an example, the vertical distribution of  $\langle u \rangle$  normalized by  $U$  at four different wave phases, in the profile at  $X = 10.842$  m (i.e., at 0.058 m upstream of the cylinder) and  $Y = 0.10$  m, for both W1 and W2. For wave W1 the phases addressed are (Figure 4a):  $t/T = 0.05$ , i.e., the wave trough;  $t/T = 0.3$ , i.e., the ascending wave phase;  $t/T = 0.65$ , i.e., the wave crest; and  $t/T = 0.8$ , i.e., the descending wave phase. Analogously, for wave W2, we have (Figure 4b):  $t/T = 0$ ,  $t/T = 0.3$ ,  $t/T = 0.55$ , and  $t/T = 0.7$ , respectively.

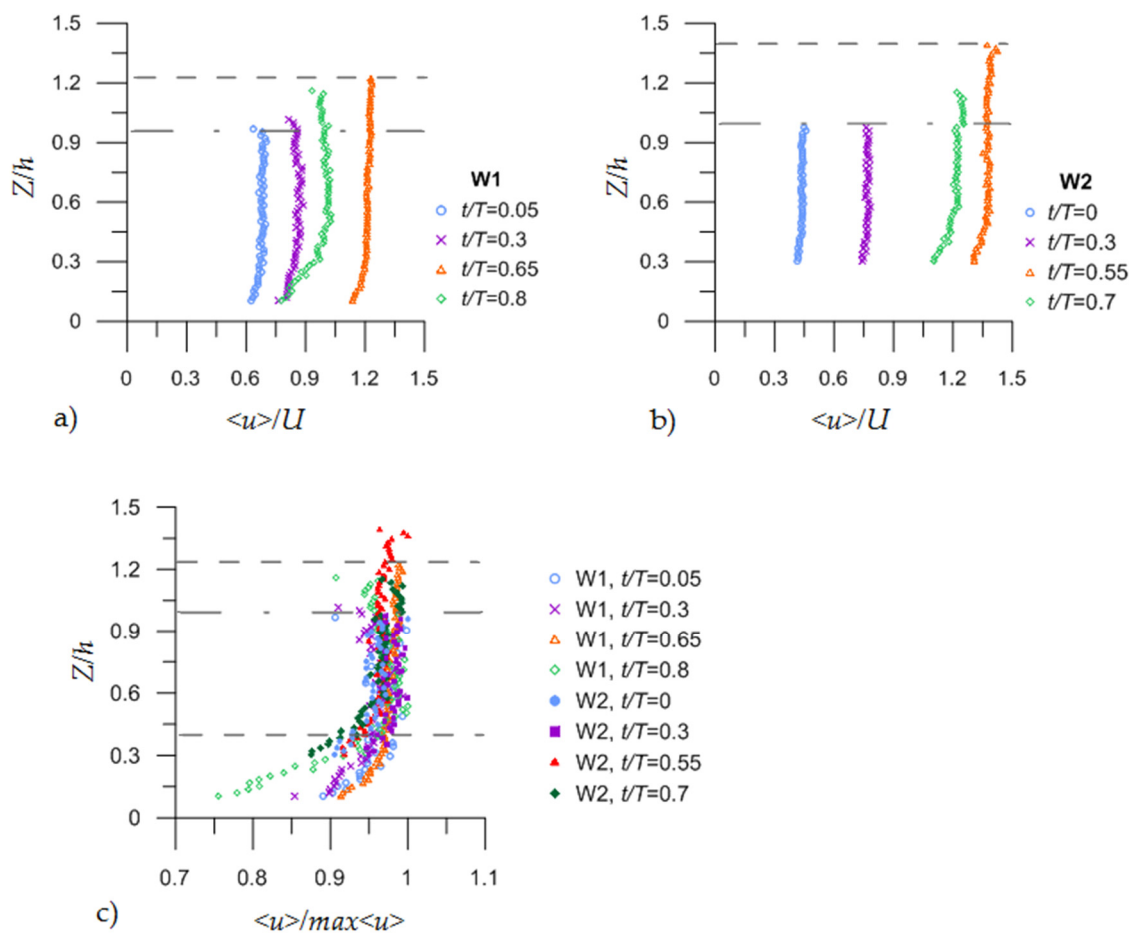


**Figure 4.** Top row: vertical profiles of the ensemble-averaged streamwise velocity  $\langle u \rangle$ , normalized by  $U$ , measured at wave trough, ascending phase, crest, descending phase. Selected profile at  $X = 10.842$  m and  $Y = 0.10$  m. (a) Wave W1 and (b) wave W2. Bottom row (c): vertical profiles of  $\langle u \rangle$  normalized by the maximum value of  $\langle u \rangle$  detected for each profile.

The vertical profiles were obtained by stitching the instantaneous velocity maps of the two FoVs upstream of the cylinder. In fact, we originally acquired a top FoV and a bottom FoV, which overlapped 0.005 m along their common edge, as plotted in Figure 2a. In particular, for the W1 wave the lower edge of the bottom FoV was positioned at  $Z = 0.01$  m, while W2 was at  $Z = 0.03$  m, in order to ensure the measurement by the PIV in the upper region during wave crest transit. This transit is evident from the increasing relative heights  $Z/h$  where velocities were measured. In fact, in the trough condition the highest point investigated is close to  $Z/h \cong 1$  in both waves, while in the crest condition, it is close to  $Z/h \cong 1.2$  for W1 and  $Z/h \cong 1.4$  for W2 consistently with the wave heights. We observed increasing values of  $\langle u \rangle$  due to the wave transit, as expected, reaching maxima values under the wave crest, with  $\langle u \rangle = 1.24U$  for W1 and  $\langle u \rangle = 1.4U$  for W2. Recalling that  $\langle u \rangle$  is the sum of the time-averaged component and the phase-averaged velocity, we can equally write that the initial current flow at most increases by about 24% and 40%, respectively, for W1 and W2 due to the wave crest transit. In addition, approaching from the trough to the crest condition, the  $\langle u \rangle$  values double for W1, while increasing 3.5 times for W2, meaning that a more pronounced effect of the wave on the underlying current is evident in the W2 case rather than in the W1 case.

Plotting the same vertical profiles of  $\langle u \rangle$  normalized by the maximum value of  $\langle u \rangle$  detected at each profile (named  $\max \langle u \rangle$ ), we obtain Figure 4c, where all profiles tend to collapse and clearly show a flat trend for  $Z/h > 0.4$ . For  $Z/h < 0.4$  the logarithmic trend of  $\langle u \rangle$  is easily recognizable, especially in the W1 case, having measured points closer to

the bottom. However, for both cases a bottom boundary layer with a thickness  $\delta \cong 0.4h$  is clearly detected, regardless of the wave phase.

### 3.3. Downstream Horizontal Maps of Streamwise Velocity and Vorticity

The horizontal maps of  $\langle u \rangle / U$  measured at  $Z = 0.03$  m are displayed in Figure 5. For the sake of brevity, only the maps corresponding to the trough and crest phases already selected and shown in Figure 4 are depicted. For greater convenience, a new local reference system  $(x, y)$  was chosen in the FoV, with the origin in the center of the cylinder.

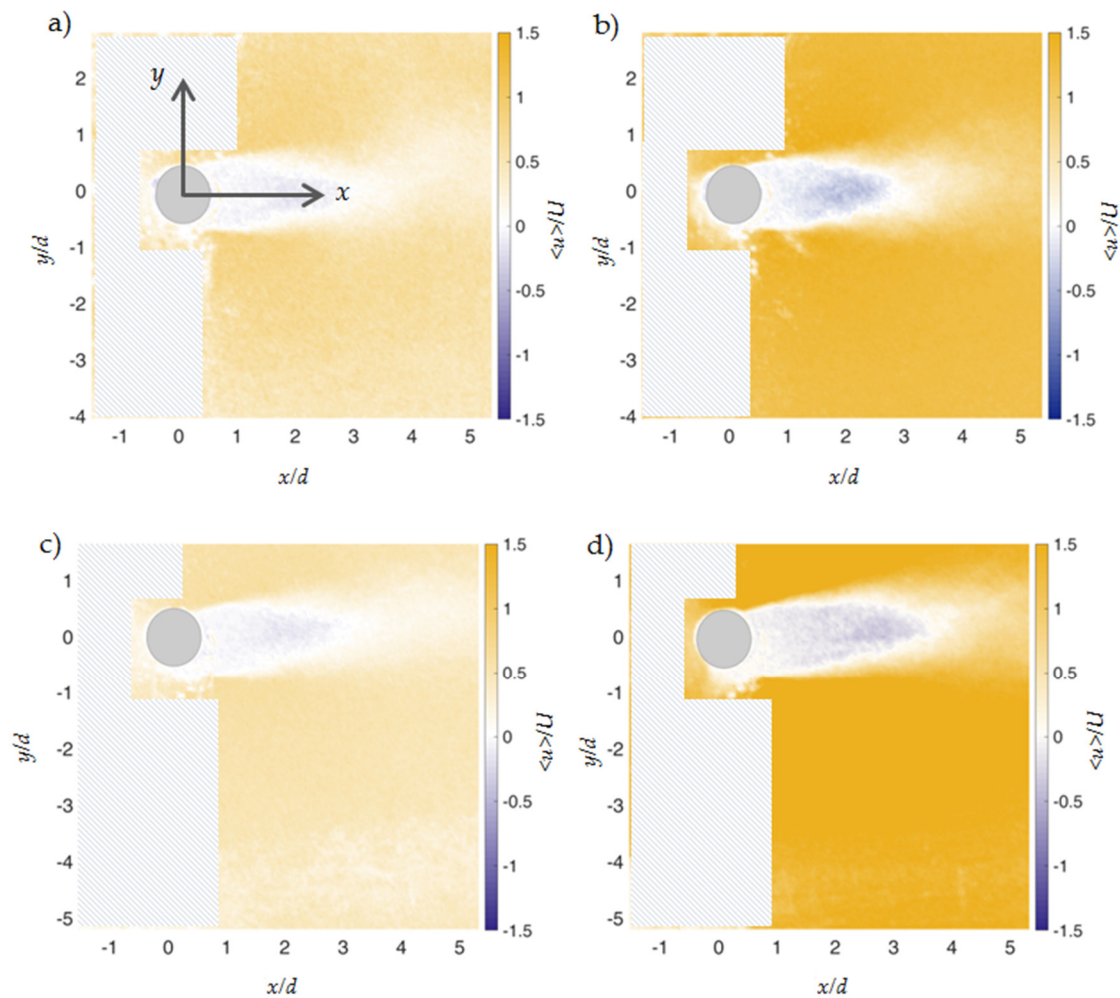


**Figure 5.** Horizontal maps of the normalized ensemble-averaged streamwise velocity  $\langle u \rangle$  at phases (a) W1 trough, (b) W1 crest, (c) W2 trough, (d) and W2 crest.  $Z$  axis is vertical and positive upward; here  $Z = 0.035$  m.

Some spurious results close to the left edge of the frame are present, due to some technical limitations in the lighting system during PIV acquisition. They do not affect the signal downstream of the cylinder in the area of greatest interest, but we decided to mask them to avoid misinterpretations. For both tests, a shaded area downstream of the cylinder is always present, as expected, showing negative  $\langle u \rangle$  values in the near wake. Due to a less intense base flow and a lower wave height in W1, the absolute values of  $\langle u \rangle$  are lower than those in W2, both in the trough (Figure 5a) and in the crest (Figure 5b). Further, the higher  $U$  value for W2 determines a more extended shaded area (Figure 5c,d). In fact we observe negative values of  $\langle u \rangle$  for  $x/d = 0 \div 3$  in the W1 case and up to  $x/d \cong 4$  in the W2 case. Instead, the transversal spreading of such negative velocities is of order  $O(d)$  for both tests. The inversion of the sign of  $\langle u \rangle$  delimits the shaded area, with values close to zero along its edge. As a result, a recirculation arises, with eddies detaching from the

cylinder and antisymmetric with respect to the local  $X$  axis, as already observed in uniform flows. However, the transit of the solitary wave, and thus the presence of a trough and a crest condition, induces a variation in the vorticity distribution and in the characteristics of coherent turbulent eddies, as explained below.

The vorticity  $\langle W_z \rangle$  in the horizontal plane at  $Z = 0.03$  m was computed starting from the ensemble-averaged streamwise  $\langle u \rangle$  and spanwise  $\langle v \rangle$  velocity components measured by the PIV. Figure 6 displays the corresponding horizontal maps for trough and crest phases, for W1 and W2, respectively.

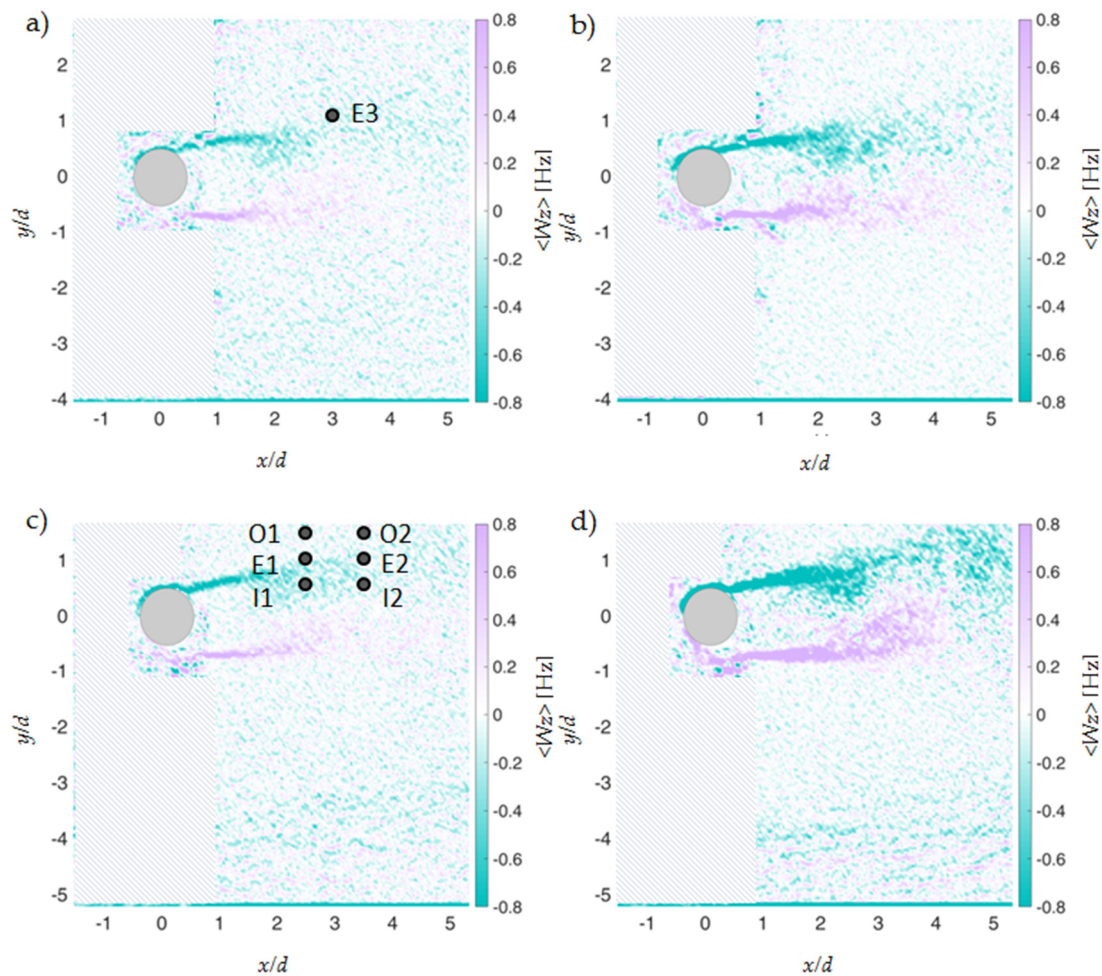


**Figure 6.** Horizontal maps of the ensemble-averaged vorticity  $\langle W_z \rangle$ , at phases (a) W1 trough, (b) W1 crest, (c) W2 trough, (d) and W2 crest. Marked points identify the locations used for the successive wavelet analysis.  $Z$  axis is vertical and positive upward; here  $Z = 0.035$  m.

Even in these plots the areas with rough data are masked, showing unreliable results. Opposite values of vorticity are observed downstream of the cylinder, mainly clockwise (negative) for  $y/d > 0$  and anticlockwise (positive) for  $y/d < 0$  consistently with the stationary case of a flow investing a cylinder. During the wave cycle, from trough to crest condition, the cylinder Reynolds number  $Re_c = \langle u \rangle d / \nu$  increases, due to the increase in  $\langle u \rangle$ , from 3400 to 6800 for W1 and from 3600 to 11,200 for W2. Thus, a more intense fully turbulent vortex street appears, as evident by comparing Figure 6a,b as well as by comparing Figure 6c,d. The antisymmetry of vorticity along the  $X$  axis is generally kept, with the highest values of  $W_z$  located at the trailing edge of the shaded area, while a spreading of vorticity with lower intensity is noted outside. In crest conditions, the values of  $W_z$  increase, especially for the W2 case where they are in the range  $(-0.8 \div 0.8)$  Hz, while for the W1 case they remain in the range  $(-0.6 \div 0.6)$  Hz.

### 3.4. Turbulent Coherent Structures

Methods based on vorticity magnitude were used fairly extensively to identify vortices in the flow. Nevertheless, it should be considered that shear layers also exhibit high vorticity magnitudes. Turbulence structures essentially evolve from the interactions between vorticity and strain rate, so in the present study, to better characterize coherent turbulent vortices in the flow, we applied the continuous wavelet transform (CWT), a power tool capable of pinpointing regions with different spatial and temporal scales in turbulent flows [24], thus providing continuous time-frequency identification of eddy structures.

Classical methods to decompose the velocity signal into frequency bands have invariably been based on the Fourier transform [25]. That is, the underlying assumption is that the same spectral components are always present in a signal. However, this approach is not particularly suited for the treatment of non-stationary signals, such as in the present case, where we distinguish and establish the length and time scales of the coherent structures residing downstream of the cylinder.

The CWT approximates a complex function as a weighted sum of simpler functions, which themselves are obtained from one simple prototype function  $\Psi$ , called the mother wavelet. Several functions can be used as the mother wavelet and we assumed the Morlet one [24,26]. In CWT, the temporal distribution of the frequency components of the signal is found by successively passing stretched and compressed versions of the function  $\Psi$ , throughout the signal. By decomposing a time series into time-frequency space, one is able to determine both the dominant modes of variability and how those modes vary in time [22].

For both waves we operated in the same way, but for convenience, we firstly focused on the results of the W2 wave. We selected six reference points in the horizontal plane (at  $Z = 0.03$  m), along two different transversal sections at relative distances  $x/d = 2.5$  and  $x/d = 3.5$ , and specifically: O1( $x/d = 2.5$ ,  $y/d = 1.5$ ), O2( $x/d = 3.5$ ,  $y/d = 1.5$ ), E1( $x/d = 2.5$ ,  $y/d = 1$ ), E2( $x/d = 3.5$ ,  $y/d = 1$ ), I1( $x/d = 2.5$ ,  $y/d = 0.5$ ), and I2( $x/d = 3.5$ ,  $y/d = 0.5$ ). Points O1 and O2 are outside the cylinder wake; points E1 and E2 are located at the trailing edge; points I1 and I2 are inside the wake (refer to Figure 6 for points location). For each point, the time series of the turbulent streamwise velocity  $u'(t)$  to be processed by CWT was obtained by stitching the  $u'(t)$  signals of the eight consecutive waves generated in the channel and cutting out the time interval between two succeeding waves. For the six target points, Figure 7a–f display the  $u'(t)$  time series, the corresponding scalogram obtained with CWT, and the global wavelet spectrum. The scalogram is the wavelet power spectrum where the highest values in the contour plot correspond to the most energetic frequencies of the signal. The black line represents the cone of influence for the wavelet, meaning that values external to such cone are untrusted because they are too close to the extremes of the time series. The global wavelet spectrum is obtained for each frequency scale from the integral of the wavelet power calculated over the period of investigation.

Considering points O1 and O2 (Figure 7a,d) in the wavelet power spectrum low intensities are generally observed, except than in the range of frequencies ( $0.0625 \div 0.25 \text{ s}^{-1}$ ) where more energetic spots are evident during most of the examined time interval. They are related to the presence of large coherent structures which retain the maximum turbulent power, as can easily be seen by observing the global wavelet spectrum. According to [24,25], we can rely on the well-known Taylor's approximation to convert the time scale  $1/f$  into the length scale  $\lambda$ . That is  $\lambda = 1/fu_s$ , where  $u_s$  is a proper velocity scale, greater than the turbulent velocity. In the present case, following [26], we assumed the local ensemble-averaged velocity  $\langle u \rangle$  as  $u_s$ , resting on the assumption that it conveys downstream of the coherent structures. As a result, the above written large coherent structures outside the wake have corresponding length scales with an order of magnitude in the range  $O(10^0 \div 10^{-1} \text{ m})$ , in particular varying between one-tenth of the wavelength  $L/10$  and the flume width  $B$ , thus controlled by the flume geometry.

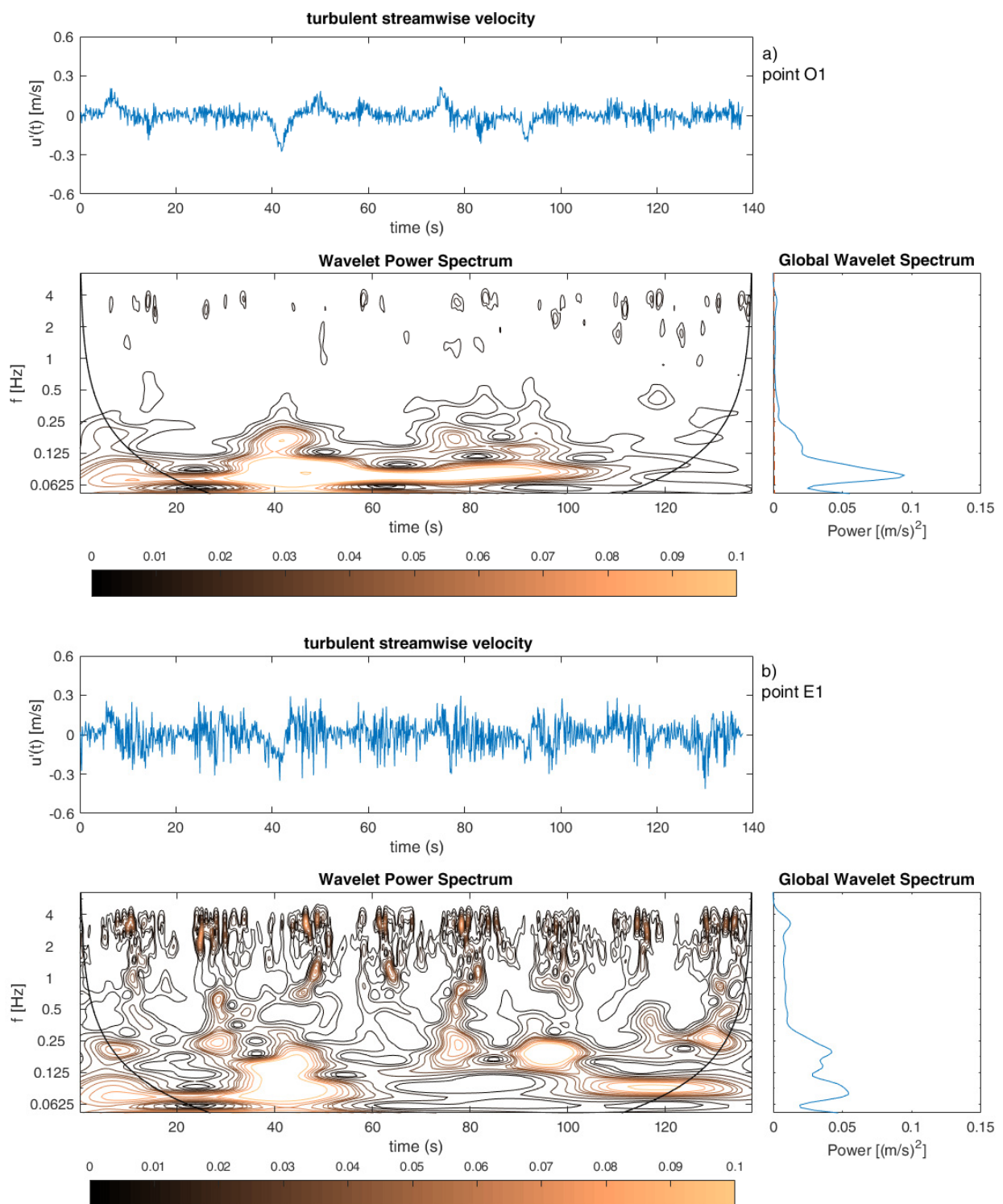


Figure 7. Cont.

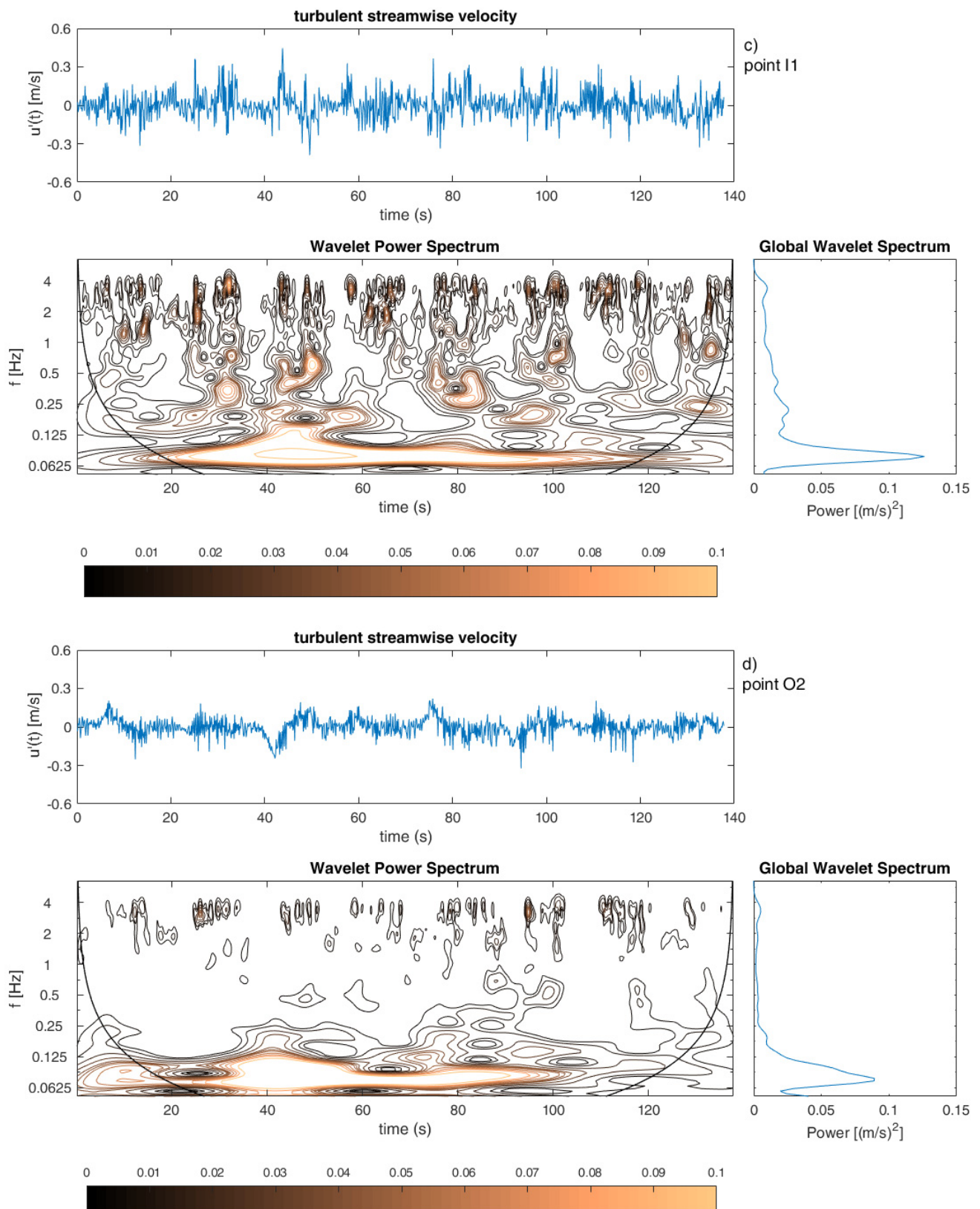
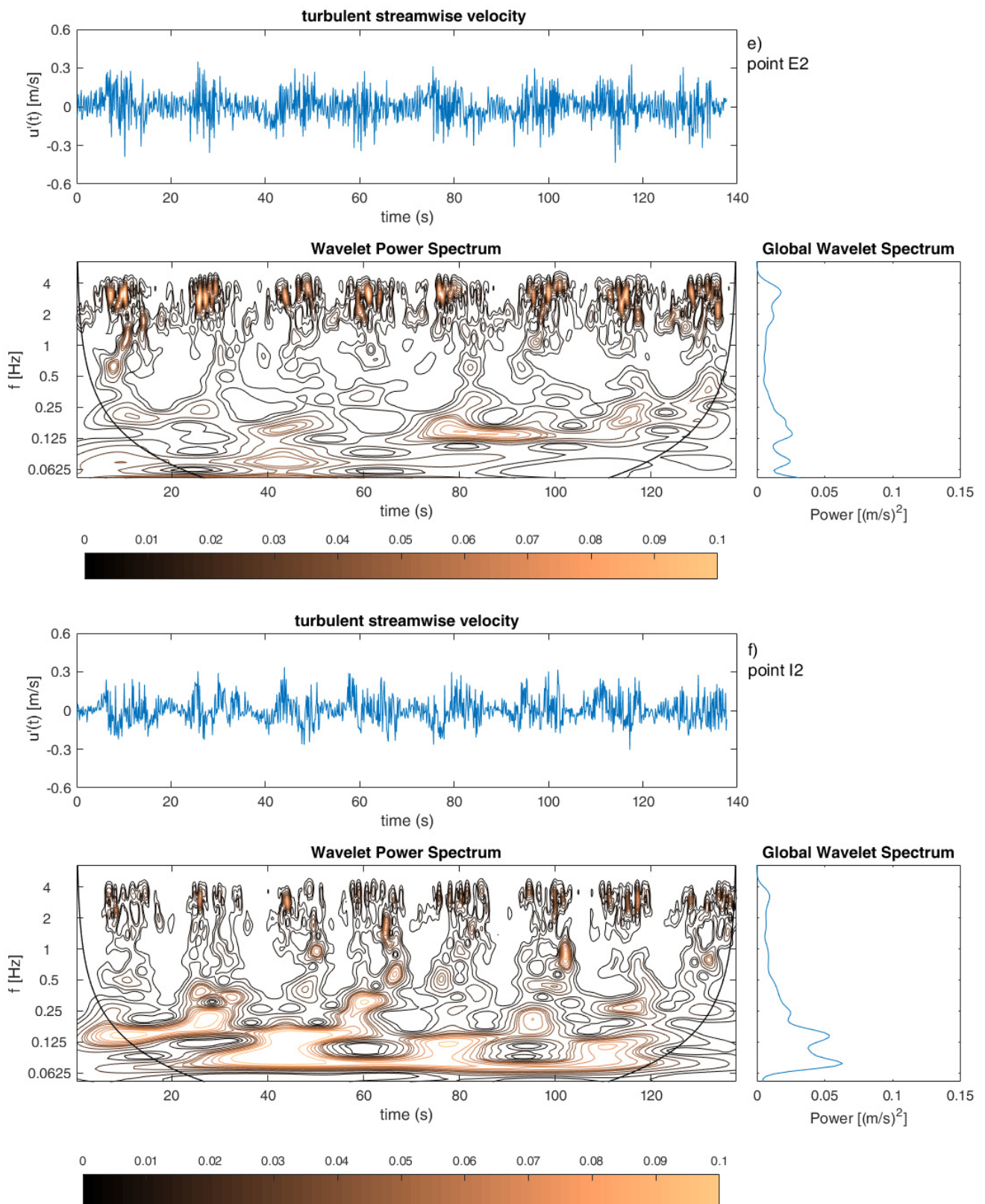


Figure 7. Cont.



**Figure 7.** W2 wave: signal of the turbulent streamwise velocity  $u'(t)$ , spectrogram of  $u'(t)$ , and global wavelet spectrum for the selected points: O1 (a), E1 (b), I1 (c), O2 (d), E2 (e), and I2 (f).

The results of the wavelet power spectrum for points E1 and E2 along the edge (Figure 7b,e) are also remarkable. Moreover, in this case, high intensities in the wavelet spectrum occur at frequencies ( $0.0625 \div 0.25 \text{ s}^{-1}$ ), manifesting again the presence of large

coherent structures similar to what was already noted for O1 and O2 points, even if characterized by lower power values. More interestingly, in E1 and E2, high power spots are visible even at higher frequencies ( $2 \div 3.5 \text{ s}^{-1}$ ), thus, we would expect them to represent small eddies. Considering that they appear only during the peak phase of the wave (as evident by moving on the time axis in Figure 7b,e), in the computation of the associated length scales we used the  $\langle u \rangle$  velocity assessed at the wave crest; therefore, their length scales result in the range ( $10^{-2} \div 10^{-1} \text{ m}$ ). More precisely, the spectrograms of Figure 7b,e show that, when the wave crest is approaching, coherent structures with the size of order of the cylinder diameter  $O(d)$  are present along the edge; during the transit of the crest, such structures become larger and are affected by the wave height with  $\lambda$  values around  $O(4H)$ .

Figure 7c,f display the CWT results for points I1 and I2 inside the wake but close to the edge, where a behavior analogous to what was already observed for points E1 and E2 is detected. In this case, the structures at frequencies ( $0.0625 \div 1 \text{ s}^{-1}$ ), present during most of the recorded time period, show again a higher turbulent power, comparable to O1 (Figure 7a) and O2 (Figure 7d) cases. The power intensity of the smaller coherent structures arising at higher frequencies ( $2 \div 3.5 \text{ s}^{-1}$ ) is quite the same as for points E1 (Figure 7b) and E2 (Figure 7e).

Referring to the coherent structures detected in the W1 case, when investigated with CWT, the turbulent power values in the spectrograms are generally halved compared with the W2 case. Nevertheless, results are similar to the W2 case in terms of frequency of occurrence of the detected coherent structures. Moreover, the order of magnitude of the length scales of the eddies is generally kept, even if their size is reduced compared with the W2 case. The reduced size of vortices behind the cylinder in the case of lower wave amplitudes was also observed by [27] for harmonic waves. For brevity, only one result for the W1 case is shown in Figure 8, referring to a representative point along the trailing edge, namely E3, at  $x/d = 3$ , and  $y/d = 1$ .

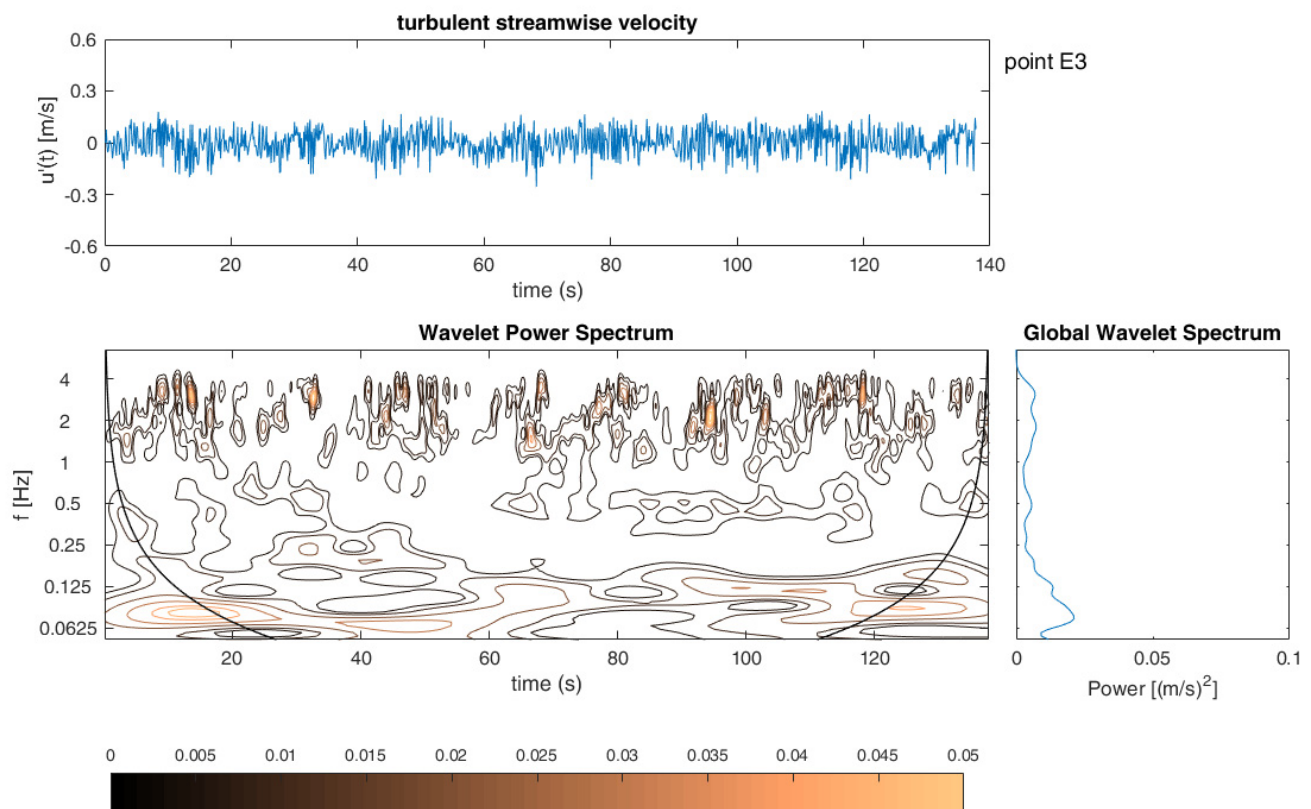


**Figure 8.** W1 wave: signal of the turbulent streamwise velocity  $u'(t)$ , spectrogram of  $u'(t)$ , and global wavelet spectrum for the selected point E3.

We can also consider the dimensionless Strouhal number  $St$  to compute the frequency of vortex shedding from the cylinder  $f_s$ . Using the local  $\langle u \rangle$  as the reference velocity scale and the diameter  $d$  as the characteristic length of the obstacle in  $St$  and posing  $St = 0.2$ , we obtain a shedding frequency varying from  $f_s \sim 2 \text{ s}^{-1}$  in absence of the wave (for both W2 and W1 cases) and  $f_s \sim 3 \text{ s}^{-1}$  for the W1 wave crest transit or  $f_s \sim 4 \text{ s}^{-1}$  for the W2 wave crest transit. Thus, such values are consistent with those of the eddies detected with the CWT method along the edge and inside the wake of the cylinder.

The global reading of the analysis conducted with the CWT reveals that the most energetic turbulent eddies in the horizontal plane, downstream of the cylinder, are large and have size varying in the range  $O(10^{-1} \div 10^0 \text{ m})$ , regardless of the position considered in the FoV. Along the edge and inside the wake other coherent structures appear at higher frequencies, consistent with the Strouhal frequency. In absence of the wave, they have the size of order of the cylinder diameter, while during the transit of the wave crest their size are of order  $O(4H)$ , i.e., they depend on the wave height. This event, occurring during the transit of the long wave crest, is in fact due to the augmented  $\langle u \rangle$  velocity produced by the wave itself.

#### 4. Conclusions

We experimentally investigated how the flow field can be modified, both upstream and downstream of a rigid, bottom-mounted, emergent cylinder, under the action of a travelling long wave. Two waves were tested, on a constant depth  $h = 0.1 \text{ m}$ ; that is W1 having a wave height of  $0.025 \text{ m}$  and W2 having a wave height of  $0.05 \text{ m}$ . Firstly, they were processed by means of the phase averaging technique and identified in analytical terms. In fact, referring to shallow water waves of great wavelength and small amplitude, we selected some solitary wave solutions that can describe the experimental waves, such as the Peregrine (PER) and the Boussinesq (BOU) solution of the KdV equation. We also compared both laboratory waves with the linear solution by Airy (LIN) and an approximate engineering method by Wheeler (WH). To evaluate the agreement in quantitative terms, the Wilmott index was considered. It resulted that for the W1 wave, the WH method is the best suiting one along the whole wave cycle. For the W2 wave, it provides the best matching in the wave trough description, while the PER model provides a better performance in the wave crest one.

After this characterization, the vertical profiles of the streamwise velocity were analyzed upstream of the cylinder, at selected and representative phases, i.e., wave trough, ascending wave, wave crest, and descending wave. In all cases a quite flat and homogeneous trend is observed, meaning that the long flooding waves promptly affected the entire water depth, from the most superficial layer towards the channel bottom. Regardless of the wave phase, a logarithmic trend with a thickness of  $0.4h$  and identifying a bottom boundary layer is recognized. For both waves, the crest transit induces an increase in the initial current flow (by about 24% for W1 and 40% for W2).

The horizontal maps of the velocity acquired at  $3 \text{ cm}$  from the bottom were then examined, evidencing a recirculation in the near wake of the cylinder, longer for W2 than for W1, due to the higher values of the streamwise velocity. The vorticity maps in the same plane highlight the presence of opposite values downstream of the cylinder, consistently with the stationary case of a flow investing a cylinder. During the wave cycle, from trough to crest condition, a more intense fully turbulent vortex street appears. The antisymmetry of vorticity along the longitudinal axis of symmetry of the cylinder is generally kept, with the highest values of vorticity located at the trailing edge of the shaded area.

Finally, to detect possible coherent structures in the same horizontal plane, the continuous wavelet transform (CWT) was applied. It shows that large coherent structures with size varying in the range  $O(10^{-1} \div 10^0 \text{ m})$  arise. They are controlled by the flume dimensions, regardless of the position downstream of the cylinder, and contain the highest turbulent energy. Along the edge and inside the wake, other smaller coherent structures appear with higher frequencies, consistent with the Strouhal frequency. In the absence of the wave, they

have length scales with order  $O(10^{-2} \text{ m})$ , i.e., comparable to the cylinder diameter, while during the transit of the wave crest their size increases, depending on the wave height, reaching order  $O(4H)$ . It is therefore evident that the long wave impacting the vertical cylinder modifies the turbulence production, spreading and dissipating downstream of the cylinder. This effect must be taken into account, as it can influence connected physical phenomena, such as entrainment and transport of sediments or tracers.

**Author Contributions:** Conceptualization and methodology, F.D.S.; supervision and funding acquisition, F.D.S.; formal analysis and investigation, R.B. and F.D.S.; writing F.D.S. All authors have read and agreed to the published version of the manuscript.

**Funding:** The research activity of RB was funded by the Italian Ministry of University and Research (Program PON RI Dottorati Innovativi con caratterizzazione industriale XXXIV ciclo, Decreto MIUR 2983/2018).

**Data Availability Statement:** The data presented in this study are available on request from the corresponding author.

**Acknowledgments:** The technical staff of the Hydraulic Laboratory of the DICATECh is gratefully acknowledged for supporting during the research activity.

**Conflicts of Interest:** The authors declare no conflict of interest. The funders had no role in the design of the study; in the collection, analyses, or interpretation of data; in the writing of the manuscript, or in the decision to publish the results.

## References

- Li, J.; Wang, Z.; Liu, S. Experimental study of interaction between multi-directional focused wave and vertical circular cylinder, part II: Wave force. *Coast. Eng.* **2014**, *83*, 233–242. [[CrossRef](#)]
- Morison, J.R.; Johnson, J.W.; Schaaf, S.A. The force exerted by surface waves on piles. *J. Pet. Technol.* **1950**, *2*, 149–154. [[CrossRef](#)]
- Zdravkovich, M.M. *Flow around Circular Cylinders. Fundamentals*; Oxford University Press: Oxford, UK, 1997; Volume 1, Chapter 6.
- Rockwell, D. Wave interaction with a vertical cylinder: Spanwise flow patterns and loading. *J. Fluid Mech.* **2002**, *460*, 93–129.
- Vested, M.H.; Carstensen, S.; Christensen, E.D. Experimental study of wave kinematics and wave load distribution on a vertical circular cylinder. *Coast. Eng.* **2020**, *157*, 103660. [[CrossRef](#)]
- Antolloni, G.; Jensen, A.; Grue, J.; Riise, B.H.; Brocchini, M. Wave-induced vortex generation around a slender vertical cylinder. *Phys. Fluids* **2020**, *32*, 042105. [[CrossRef](#)]
- Duan, W.J.; Wang, Z.; Zhao, B.B.; Ertekin, R.C.; Yang, W.Q. Steady solution of solitary wave and linear shear current interaction. *Appl. Math. Model.* **2018**, *60*, 354–369. [[CrossRef](#)]
- Chen, Y.H.; Wang, K.H. Experiments and computations of solitary wave interaction with fixed, partially submerged, vertical cylinders. *J. Ocean Eng. Mar. Energy* **2019**, *5*, 189–204. [[CrossRef](#)]
- Mo, W.; Jensen, A.; Liu, P. Plunging solitary wave and its interaction with a slender cylinder on a sloping beach. *Ocean Eng.* **2013**, *74*, 48–60. [[CrossRef](#)]
- Huang, Z.; Yuan, Z. Transmission of solitary waves through slotted barriers: A laboratory study with analysis by a long wave approximation. *J. Hydro-Environ. Res.* **2010**, *3*, 179–185. [[CrossRef](#)]
- Maza, M.; Lara, J.M.; Losada, I.J. Solitary wave attenuation by vegetation patches. *Adv. Water Res.* **2016**, *98*, 159–172. [[CrossRef](#)]
- Yang, Z.; Huang, B.; Kang, A.; Zhu, B.; Han, J.; Yin, R.; Li, X. Experimental study on the solitary wave-current interaction and the combined forces on a vertical cylinder. *Ocean Eng.* **2021**, *236*, 109569. [[CrossRef](#)]
- Kim, S.Y.; Kim, K.M.; Park, J.C.; Jeon, G.M.; Chun, H.H. Numerical simulation of wave and current interaction with a fixed offshore substructure. *Int. J. Nav. Arch. Ocean Eng.* **2016**, *8*, 188–197. [[CrossRef](#)]
- Ben Meftah, M.; De Serio, F.; De Padova, D.; Mossa, M. Hydrodynamic structure with scour hole downstream of bed sills. *Water* **2020**, *12*, 186. [[CrossRef](#)]
- Olsen, N.R.B.; Melaaen, M.C. Three-dimensional calculation of scour around cylinders. *J. Hydr. Eng.* **1993**, *119*, 1048–1054. [[CrossRef](#)]
- Nepf, H.M. Flow and transport in regions with aquatic vegetation. *Annu. Rev. Fluid Mech.* **2012**, *44*, 123–142. [[CrossRef](#)]
- De Serio, F.; Mossa, M. A laboratory study of irregular shoaling waves. *Exp. Fluids* **2013**, *54*, 1536. [[CrossRef](#)]
- Bi, C.W.; Zhao, Y.P.; Dong, G.H.; Xu, T.J.; Gui, F.K. Experimental investigation of the reduction in flow velocity downstream from a fishing net. *Aquac. Eng.* **2013**, *57*, 71–81. [[CrossRef](#)]
- CERC. *Shore Protection Manual*; U.S. Army Corps of Engineers: Washington, DC, USA, 1984; Volume 1.
- Hereman, W. Shallow Water Waves and Solitary Waves. In *Encyclopedia of Complexity and Systems Science*; Meyers, R.A., Ed.; Springer: Berlin, Germany, 2018; pp. 1–18.

21. Madsen, P.A.; Fuhrman, D.R.; Schäffer, H.A. On the solitary wave paradigm for tsunamis. *J. Geophys. Res. Oceans* **2008**, *113*, 012. [[CrossRef](#)]
22. De Serio, F.; Mossa, M. Assessment of classical and approximated models estimating regular waves kinematics. *Ocean Eng.* **2016**, *126*, 176–186. [[CrossRef](#)]
23. De Padova, D.; Brocchini, M.; Buriani, F.; Corvaro, S.; De Serio, F.; Mossa, M.; Sibilla, S. Experimental and Numerical Investigation of Pre-Breaking and Breaking Vorticity within a Plunging Breaker. *Water* **2018**, *10*, 38722. [[CrossRef](#)]
24. Torrence, C.; Compo, G.P. A practical guide to wavelet analysis. *Bull. Am. Meteorol. Soc.* **1998**, *79*, 61–78. [[CrossRef](#)]
25. Kanani, A.; da Silva, A.M.F. Application of continuous wavelet transform to the study of large-scale coherent structures. *Environ. Fluid Mech.* **2015**, *15*, 1293–1319. [[CrossRef](#)]
26. Longo, S. Turbulence under spilling breakers using discrete wavelets. *Exp. Fluids* **2003**, *34*, 181–191. [[CrossRef](#)]
27. Muddada, S.; Hariharan, K.; Sanapala, V.S.; Patnaik, B.S.V. Circular cylinder wakes and their control under the influence of oscillatory flows: A numerical study. *J. Ocean Eng. Sci.* **2021**, *6*, 389–399. [[CrossRef](#)]